

Ultrafast to Ultraslow Dynamics of a Langmuir Monolayer at the Air/Water Interface Observed with Reflection Enhanced 2D IR Spectroscopy

Chang Yan, Joseph E. Thomaz, Yong-Lei Wang, Jun Nishida, Rongfeng Yuan, John P. Breen and Michael D. Fayer*

Department of Chemistry
Stanford University, Stanford, CA 94305
Phone: 650 723-4446; Email: fayer@stanford.edu

Supporting Information

1. Preparation of Rhenium(I) Diimine Complexes

4,5-diazafluoren-9-one (97% Sigma Aldrich), octadecylamine (97% Sigma Aldrich), 2,2'-bipyridine-4,4'-dicarboxylic acid (98% Sigma Aldrich), *p*-toluenesulfonic acid monohydrate (98.5% Sigma Aldrich), rhenium(I) pentacarbonyl chloride (98% STREM Chemical), sodium hydroxide (>98% Fisher Chemical), benzene (99.8% Sigma Aldrich), toluene (99.9% Fisher Chemical), petroleum ether (boiling point range 36~56 °C, Fisher Chemical), *n*-heptane (reagent grade, Fisher Chemical), methanol (99.9% Fisher Chemical), chloroform (99.9% Fisher Chemical), dichloromethane (99.9% Fisher Chemical), deuterated chloroform (99.8% atom % D, Acros), *d*⁶-dimethyl sulfoxide (99.9% atom % D, Acros), deionized ultra-filtered H₂O (Fisher Chemical), and deuterium oxide (99.9 atom % D, Sigma Aldrich) were purchased from their listed vendors and used without further purification. Proton nuclear magnetic resonance (NMR) spectra were collected on an Inova 300 MHz spectrometer with chemical shifts reported relative to tetramethylsilane. Mass spectra were recorded on a Micromass ZQ single quadrupole system using the electrospray ionization (ESI) method.

fac-tricarbonylchloro-9-octadecylamino-4,5-diazafluorenerhenium(I) (**TReF18**), was synthesized and purified by recrystallization according to a previous report.¹ ¹H NMR (CDCl₃): δ 8.82 (t, 2H), 8.32 (t, 2H), 7.61 (m, 2H), 4.26 (t, 2H), 1.97 (m, 2H), 1.28 (m, 30H), 0.90 (t, 3H). ESI-MS *m/z*: 704 ($\{M - Cl\}^+$).

fac-tricarbonylchloro-2,2'-bipyridine-4,4'-dicarboxylrhenium(I) was synthesized according to a published procedure². ¹H NMR (*d*⁶-DMSO): δ 9.22 (d, 2H), 9.15 (s, 2H), 8.14 (d, 2H). ESI-MS *m/z*: 547. The corresponding dilute ~1 mM sodium salt aqueous solution, referred as TReBDC, was prepared by dissolving the neutral complex in a D₂O/NaOH solution. The pH of the final solution was 12.3.

The three carbonyl peaks for TReBDC in D₂O are at 2016, 1908, 1892 cm⁻¹. The three carbonyl peaks for TReF18 in CHCl₃ are at 2031, 1932, 1904 cm⁻¹. The 2031 cm⁻¹ symmetric stretch mode of TReF18 in chloroform has an extinction coefficient of 5900 M⁻¹cm⁻¹.

2. Maintaining the Water Level with a Feedback Loop System

During the 2D IR measurements spanning several hours, the water surface level had to be precisely maintained to avoid optical misalignment and change of the meniscus shape. The water level was monitored in real time by aiming a collimated 20 mW continuous-wave 650 nm diode laser beam (diameter = 5 mm) onto the water surface.

About 2 mW of the beam was reflected off the surface and passed into a Thorlabs PDQ80A quadrant detector. The laser frequency was chosen to avoid the visible absorption band of TReF18.¹ At the beginning of each experiment the initial water level was measured by the detector and used as a reference point for the remainder of the experiment. A New Era Pump Systems NE-1000 stepper motor pump was then set to inject water at an initial rate estimated to be near that of the average rate of water evaporation. Tygon tubing connected the pump to a needle. The needle tip passed through a hole made in the wall of the petri dish, which allowed ultrapure water (resistivity > 18 M Ω cm) to be slowly pumped into the dish without disturbing the water surface. The average water level measured by the quadrant detector was used as the input information for a proportional feedback algorithm to alter the injection rate of the pump every 30 seconds. With these considerations it became possible to maintain the water level constant within $\pm 2 \mu\text{m}$.

3. Atomistic Molecular Dynamics Simulations

Quantum mechanics (QM) *ab initio* calculations were first performed to obtain optimized molecular geometries with the Gaussian 09 package.³ The molecular structure of a single TReF18 head group was optimized using density functional (DFT) theory with Becke's three-parameter hybrid functional combined with Lee-Yang-Parr correlation functional forms.^{4,5} The LANL2DZ pseudopotential was used to treat the rhenium atom, and the 6-31+g(d,p) basis set was applied for all other light atoms.⁶ Partial atomic charges were derived from optimized molecular geometries with the restraint electrostatic potential (RESP) fitting approach by fitting the molecular electrostatic potential generated from QM *ab initio* calculations. The atomistic force field parameters for TReF18 molecules were taken from previous work based on the CHARMM framework.^{6,7} The cross-interaction Lennard-Jones parameters between different types of atoms were obtained from Lorentz-Berthelot combining rules. The simulation box is shown in Figure S1. For the self-assembled TReF18 molecules on water surface, a simulation box consisting of 5333 TIP3P water molecules was pre-equilibrated in a cubic box with dimensions of $9.0 \times 9.0 \times 2.1 \text{ nm}^3$.

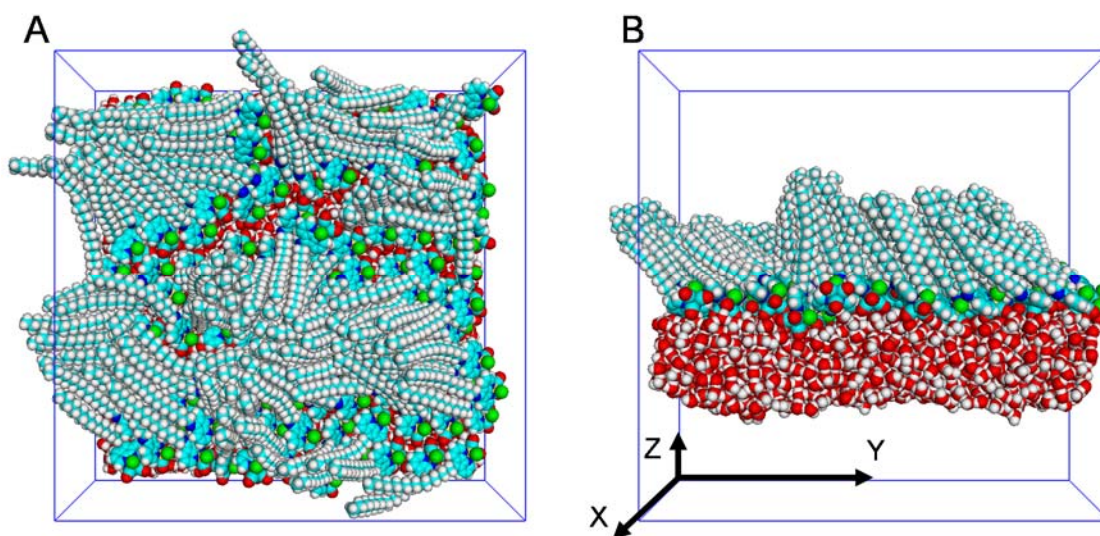


Figure S1. The MD simulation box viewed from top (A) and side (B).

There were 132 TReF18 molecules on the water surface. The corresponding mean molecular area was 0.61 nm^2 per TReF18 molecule. Atomistic molecular dynamics simulations were performed using *M.DynaMix* package⁸ with three-dimensional periodic boundary condition. The periodic distance in the Z axis, which was perpendicular to the water surface, was set to 12.0 nm, which is sufficiently large to ensure that interactions between terminal carbon atoms of adsorbed TReF18 molecules and the periodic image of the water molecules can be ignored. The equations of motion were integrated using the Tuckerman-Berne double time step algorithm with short and long time steps of 0.1 and 1.0 fs, respectively. The short time step was used for integrating fast intramolecular vibrations and nonbonded interactions within 0.5 nm, while the long time step was used for integrating van der Waals and electrostatic interactions within 1.5 nm, as well as the dihedral angle motions. The electrostatic interactions between atom-centered point charges are treated with the standard Ewald summation method. The simulation system was first equilibrated for 10 ns in NVT ensemble at 300 K maintained using Nosé-Hoover thermostat with the time coupling constant of 500 fs. Canonical ensemble simulations were further performed for 16 ns, and simulation trajectories were recorded at an interval of 200 fs for further structural analysis.

4. Quantum Chemical Calculations for Determining Carbonyl Vibrational Frequencies

The electronic structures of TReBDC and TReF18 were optimized in vacuum by DFT methods based on the same set of functional forms and basis sets as the DFT calculations performed before MD simulations. The electron density maps of the two complexes are shown in Figure S2A. Due to the negative charges contributed by the two carboxylate groups, the carbonyls in TReBDC have a higher electron density than the carbonyls in TReF18. The higher electron density occupies the anti-bonding orbitals of the carbonyls, shifting the symmetric stretching mode of TReBDC towards redder frequencies as compared with TReF18. The carbonyl symmetric stretch mode vibrational frequencies of TReBDC and TReF18 were calculated by DFT methods with Gaussian 09 in a range of implicit solvent environments using the polarizable continuum model (PCM). The calculated frequencies are shown in Figure S2B. Under the same solvent environment, the TReBDC frequency is consistently lower than that of TReF18. The calculated frequency of TReBDC in water is 14.7 cm^{-1} lower than that of TReF18 in chloroform. The measured frequencies are 2016 cm^{-1} for TReBDC in D_2O and 2031 cm^{-1} for TReF18 in chloroform, and the difference is 15 cm^{-1} . The calculated frequency difference matches experimental results exceedingly well. Therefore, the red-shifted vibrational frequencies of TReBDC in D_2O in comparison with TReF18 monolayers on water surface are mainly caused by the difference of electronic structures of the two complexes.

Atomistic MD simulations indicate that carbonyl groups in TReF18 molecules exhibit different hydrogen bonding configurations with water molecules at the water surface. The criteria used for identifying a hydrogen bond here is the O-O distance between a water oxygen and a carbonyl oxygen is less than 2.50 Å and the hydrogen bond angle is between 150° and 180°. It was found that the three carbonyls in a TReF18 molecule form 0~6 hydrogen bonds with surrounding waters. The histogram for the

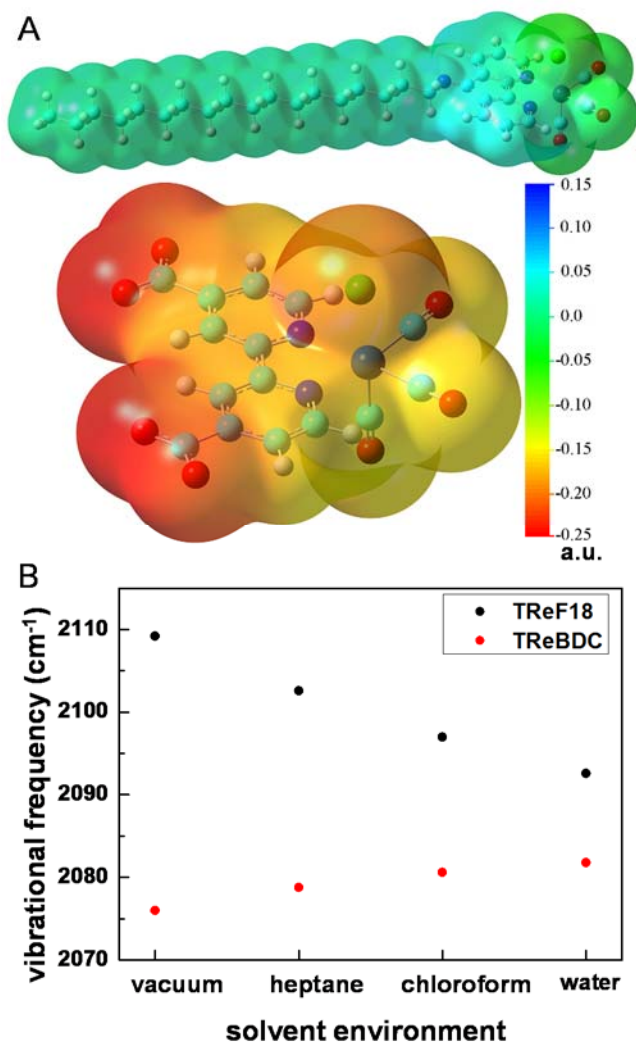


Figure S2. (A) Electron density map of TReBDC and TReF18. (B) Carbonyl symmetrical stretch frequencies calculated in different implicit solvent models.

configurations are shown in the main text Figure 6A.

To investigate the effect of water-carbonyl hydrogen bonding on the vibrational frequency of carbonyl symmetrical stretch mode, typical structures consisting of one TReF18 molecule and 6 neighboring water molecules were taken from simulations trajectories and used as starting configurations in the subsequent quantum chemistry calculations. Examples of these configurations are presented in Figure S3. In the vibrational frequency calculations, the electronic structure of TReF18 and waters were fine-tuned based on the same set of functional forms and basis sets as the previous DFT

calculations, and then the vibrational frequencies of carbonyl groups were determined (Figure 6B in main text).

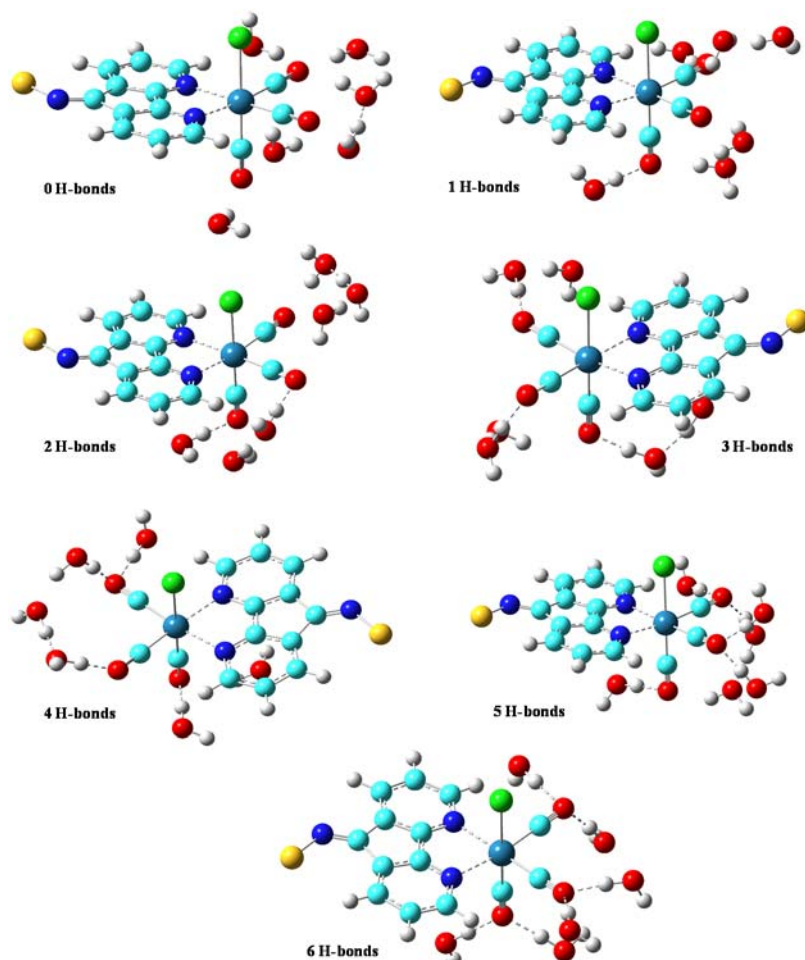


Figure S3. Hydrogen bonding configurations between TReF18 and the closest 6 surrounding water molecules. Yellow – C₁₈H₃₇ alkyl chain, blue – nitrogen, cyan – carbon, grey – hydrogen, red – oxygen, green – chlorine, light blue – rhenium. Hydrogen bonds between water and TReF18 are represented by dash lines between carbonyl oxygen atoms and water hydrogen atoms.

5. FT-IR Spectra of a TReF18 Supersaturated Bulk Solution with the Main Structure Peak and the Two Minor Structure Peaks

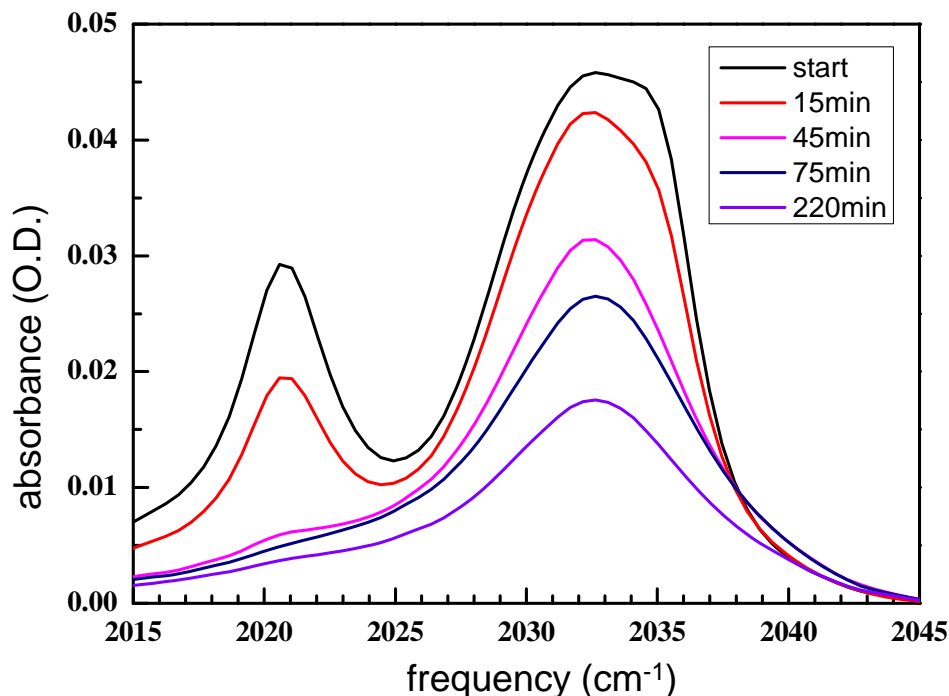


Figure S4. Time-independent FT-IR spectra of TReF18 in CHCl₃/heptane (1:10 volume:volume) solution.

0.1 mL of 20 mM TReF18 solution in chloroform was injected into 1 mL of heptane, and the mixed solution was filtered to obtain a transparent supersaturated solution before measurements. The sample path length was 100 μm . At the start, the solution exhibited three peaks similar to the case in HD monolayer: red minor peak at 2021 cm^{-1} , main peak at 2032 cm^{-1} , and blue minor peak at $\sim 2036 \text{ cm}^{-1}$ merging with the main peak. As time increased, TReF18 gradually precipitated out from the solution. The main structure peak and the two minor structure peaks in the solution all decreased in amplitude, but the minor structure peaks decreased much more prominently. As the concentration of TReF18 dropped by $\sim 50\%$ at 75 minutes, the minor structure peaks completely disappeared. TReF18 only exhibited one peak in chloroform, even at a high concentration of 20 mM. The appearance of minor peaks required an unfavorable solvent as well as high concentration, suggesting that the minor structures may be related to the formation of dimers, intermolecular oligomers of TReF18 molecules or strong intermolecular interactions from the close proximity of the molecules.

6. 2D IR Spectra of LD Monolayer at $T_w = -100$ ps and 100 ps.

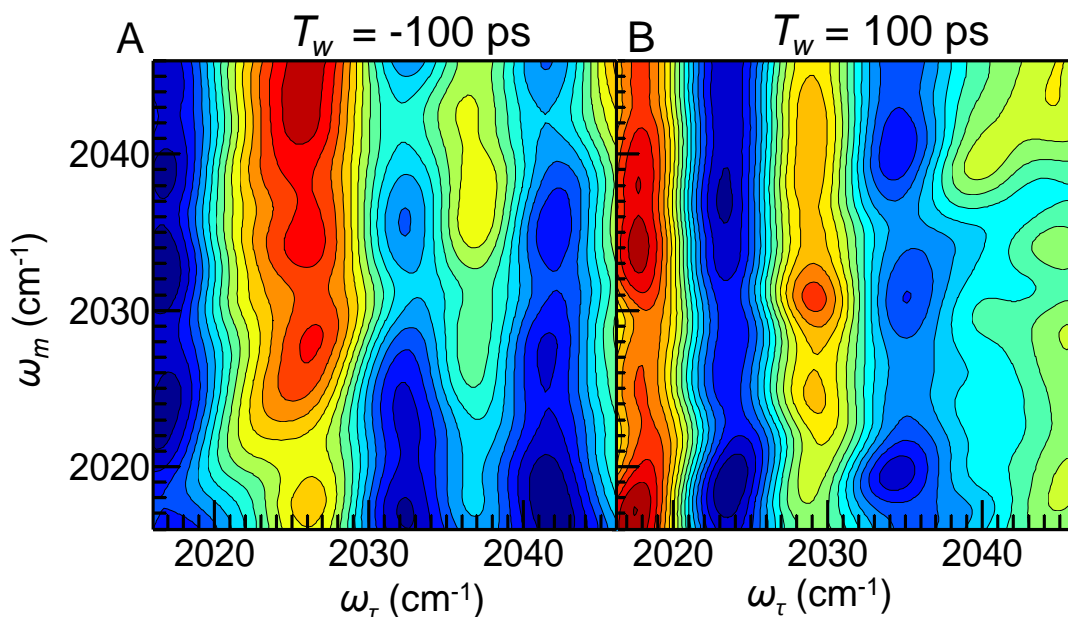


Figure S5. The 2D IR spectra at $T_w = -100$ ps and 100 ps only showed low-amplitude noise stripes, and therefore water heating artifacts were not present in the 2D IR spectra measured at the frequencies of TReF18 symmetrical stretch mode. The amplitude of the noise is $\sim 0.5\%$ of the resonant signal at $T_w = 0.6$ ps, or $\sim 5\%$ of the resonant signal amplitude at $T_w = 30$ ps.

7. Ultraslow Structural Evolution Measured under Dust-free Ambient Air versus under Ultrapure Nitrogen Purge.

In Figure S6, we present the center line slope at $T_w = 0.6$ ps measured at different times after monolayer deposition. The CLS change measured under 99.999% nitrogen purge or under ambient air is compared for LD monolayer (6A) sample and HD monolayer sample (6B). For both LD and HD monolayers, the CLS value increases for 5~7 hours before reaching a relatively stable plateau region regardless of the atmosphere used. Therefore, the evolution cannot be caused by slow build-up of air-borne contaminants on the water surface.

For monolayers exposed to ambient air, the humidity around the sample is $\sim 35\%$, the water evaporation rate is ~ 1.7 mL/hour, and the water temperature is 21.2 °C. For monolayers sealed in the box and purged with 99.999% nitrogen, the water vapor was trapped in the box but purged away constantly by the nitrogen. The water evaporation rate is reduced to ~ 0.8 mL/hour, and the water temperature is 22.5 °C.

The results measured with or without nitrogen purge in Figure 6A and 6B are fundamentally similar in terms of the trend of change of CLS. The small differences might arise from the different temperature and humidity during measurements. Note that

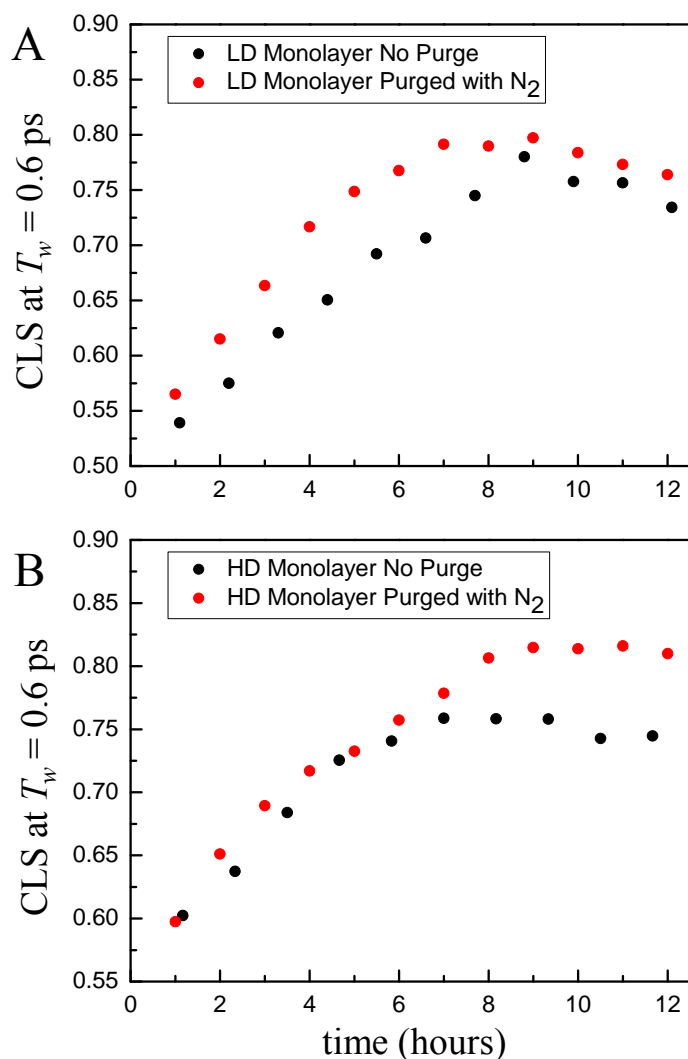


Figure S6. The ultraslow evolution of CLS at $T_w = 0.6$ ps measured under dust-free air or ultrapure nitrogen.

the vertical scale is greatly expanded compared to the full range that runs from 0 to 1. There are small differences in the data, but the overall trends are the same.

8. Estimation of Heating Caused by IR Pulses.

The output of the OPA is about 90 mW with a repetition rate of 3 kHz. Due to the diffraction efficiency of the AOM pulse shaper, the total IR power illuminated on the water surface under our experimental condition is about 32.5 mW as measured by an optical power meter. This corresponds to a pulse energy of 10.8 μ J per pulse. The Gaussian profile IR beam was focused and incident on the water surface with an angle of 45° . The beam at the focus was measured by a pinhole to have a radius $w_0 = 100$ microns. That is, 86.5% of the total IR power passes through the circle with a radius of 100 microns. Taking the shape of projected oval onto the water surface into account, 28 mW of IR power, or 9.3 μ J per pulse, was shined onto an oval with an area of 4.4×10^{-4}

cm². For convenience, we count the pump and the probe beams as a single one with the combined power here.

Almost all of the IR power is absorbed by water, since the monolayer itself only has an absorbance ~ 0.002 O.D. At 2030 cm⁻¹, it takes a path length of 12 microns for water's background IR absorbance to reach 0.3 O.D. which corresponds to absorbing 50% of the IR energy. The volume of the tilted cylinder that the IR beam travels into the water with a path length of 12 microns is calculated to be 3.77×10^{-7} mL. Therefore, a single input 9.3 μ J IR pulse during our measurement will raise the first 12 microns of water by 3 °C. In the same way, we can calculate that for the first 100 nm of water, the temperature will raise by 4 °C.

The laser pulse arrives every 0.33 ms. The thermal diffusivity of water is 14.6 Å²/ps, which is 14.6×10^{-4} cm²/s. The root mean square displacement of the heat after 0.33 ms can be calculated as 9.8 μ m, cooling down the initial temperature rise to about 1.8 °C. We can iterate the process for the next laser shots. After ~ 10 shots, the temperature rise converges to a value of ~ 6 °C.

In the experiments with the dish exposed to air, the water temperature in the dish is 21 °C as measured by a thermal couple probe tested in multiple positions in the water. This is slightly lower than the room temperature 23.5 °C as a result of water evaporation. The evaporation rate of water in our specific setting is 1.7 mL per hour as measured by the precise syringe pump in the feedback system discussed in the paper. Taking the water evaporation enthalpy to be 40.65 kJ/mol, the cooling power due to evaporation is 1 Watt, which is about 40 greater than heating from the power deposited by the laser. Therefore, the IR absorption is not affecting the thermal equilibrium of the entire water body in the dish and the monolayer on it. Within the laser spot, as calculated above, the temperature is $21 + 6 = 27$ °C, which is a typical temperature for measuring water spectral diffusion dynamics. For experiments under nitrogen purge, the water evaporation rate is 0.8 mL per hour, and the water temperature is 22.5 °C. Then the water temperature within the laser spot is $22.5 + 6 = 28.5$ °C.

The IR laser pulse energy does not affect the CLS data. When the laser pulse energy was reduced by 30%, the same experimental results were obtained.

We have shown the 2D IR spectra acquired at $T_w = 100$ ps and $T_w = -100$ ps in the Figure S5. Both spectra display a low noise level with an amplitude that is $\sim 0.5\%$ of the resonant signal at $T_w = 0.6$ ps, or $\sim 5\%$ of the resonant signal amplitude at $T_w = 30$ ps. The 2D IR spectra demonstrate that there are neither interfering heating background within 100 ps nor between laser shots.

Since the temperature within the spot converges to equilibrium within ~ 10 shots (3.3 ms), the 2D IR spectral fluctuations on the timescale of seconds and minutes observed in the higher density monolayer cannot be due to thermal fluctuations caused by laser pulses. The laser pulses are very stable with shot to shot fluctuations of less than 1% standard deviation.

References

1. V. W. W. Yam, K. Z. Wang, C. R. Wang, Y. Yang, K. K. Cheung, *Organometallics* **1998**, *17*, 2440-2446.
2. J. M. Smieja, C. P. Kubiak, *Inorg. Chem.* **2010**, *49*, 9283-9289.

3. M. J. Frisch, G. W. Trucks, H. B. Schlegel, G. E. Scuseria, M. A. Robb, J. R. Cheeseman, G. Scalmani, V. Barone, G. A. Petersson, H. Nakatsuji, X. Li, M. Caricato, A. Marenich, J. Bloino, B. G. Janesko, R. Gomperts, B. Mennucci, H. P. Hratchian, J. V. Ortiz, A. F. Izmaylov, J. L. Sonnenberg, D. Williams-Young, F. Ding, F. Lipparini, F. Egidi, J. Goings, B. Peng, A. Petrone, T. Henderson, D. Ranasinghe, V. G. Zakrzewski, J. Gao, N. Rega, G. Zheng, W. Liang, M. Hada, M. Ehara, K. Toyota, R. Fukuda, J. Hasegawa, M. Ishida, T. Nakajima, Y. Honda, O. Kitao, H. Nakai, T. Vreven, K. Throssell, J. A. Montgomery, Jr., J. E. Peralta, F. Ogliaro, M. Bearpark, J. J. Heyd, E. Brothers, K. N. Kudin, V. N. Staroverov, T. Keith, R. Kobayashi, J. Normand, K. Raghavachari, A. Rendell, J. C. Burant, S. S. Iyengar, J. Tomasi, M. Cossi, J. M. Millam, M. Klene, C. Adamo, R. Cammi, J. W. Ochterski, R. L. Martin, K. Morokuma, O. Farkas, J. B. Foresman, and D. J. Fox, *Gaussian 09 Revision A.1.*; Gaussian Inc.: Wallingford, CT, 2009.
4. A. D. Becke, *Phys. Rev. A* **1988**, *38*, 3098-3100.
5. C. Lee, W. Yang, R. G. Parr, *Phys. Rev. B* **1988**, *37*, 785-789.
6. C. Yan, R. Yuan, W. C. Pfalzgraff, J. Nishida, L. Wang, T. E. Markland, M. D. Fayer, *Proc. Natl. Acad. Sci. U.S.A.* **2016**, *113*, 4929-4934.
7. K. Vanommeslaeghe, E. Hatcher, C. Acharya, S. Kundu, S. Zhong, J. Shim, E. Darian, O. Guvench, P. Lopes, I. Vorobyov, A. D. Jr. Mackerell, *J. Comput. Chem.* **2010**, *31*, 671-690.
8. A. P. Lyubartsev, A. Laaksonen, *Comput. Phys. Commun.* **2000**, *128*, 565-589.